

The Role of Geometry-constrained Forces in Morphogenesis

Jesús Fuentes* and María Moscardó García

*Luxembourg Centre for Systems Biomedicine,
University of Luxembourg, Belvaux L-4367, Luxembourg*

Jorge Gonçalves

*Luxembourg Centre for Systems Biomedicine,
University of Luxembourg,
Belvaux L-4367, Luxembourg and
Department of Plant Sciences,
Cambridge University,
Cambridge CB2 3EA, United Kingdom*

Morphogenesis, a pivotal process in developmental biology, remains challenging to dissect due to the difficult interaction of mechanical forces, cellular dynamics, and unique topologies. Considering these complexities, we introduce a novel framework to study the interplay between geometry-constrained forces and morphogenetic processes. Our model integrates mechanical and geometric forces, stochastic movements, and key cellular life events, excelling in simulating cell-cell interactions in dynamic open biological systems. Significantly, it incorporates tissue or background geometry, representing genetic information influencing patterning and morphogenesis. This enables our model to replicate the natural heterogeneity and complexity observed in authentic tissue structures. Numerical simulations, demonstrate the model's broad applicability across diverse morphologies. Our model holds as a potential tool for hypothesis generation in therapeutic research, with implications for tissue engineering, oncology, and regeneration studies.

I. INTRODUCTION

Morphogenesis, a cornerstone in developmental biology, governs the spatial configuration of cells to form tissues and organs with functional integrity [1]. This process manifests through a series of continuous transformations, culminating in distinct structural formations [2]. Beyond its role in embryonic development, morphogenesis extends its influence into mature organisms, where it regulates tissue homeostasis and facilitates the regeneration of damaged structures. The elucidation of the mechanisms by which a cellular collective achieves its final structural conformation presents an interdisciplinary challenge at the intersection of physics and developmental biology.

Morphogenesis can be perceived as a process in which chemical and mechanical properties generate stresses and strains. These, in turn, stimulate cellular movement, enabling cells to alter their shape, divide, and reposition themselves. The cytoskeleton, for example, is frequently attributed a pivotal role in generating internal stress, while the actin cortex partakes in the creation of surface tensions along cell membranes [3]. Such mechanical factors, instigated by genetic programmes, result in a diverse array of tissue and organism shapes. Bridging the gap between patterning, mechanics and morphogenesis, as highlighted by Liu et al. [4], is the next challenge in the field.

Physics-based models attempt to provide insights into the mechanisms of morphogenesis by capturing repres-

entative mechanical forces acting within and between cells, as well as the cellular responses to various environmental and geometric influences [5]. These models hinge on assumptions about the interactions and forces at play in cell sheets, individual cells, or intercellular relationships to interpret the shapes observed *in vivo*. For instance, single cells may adjust their migratory behaviour in response to environmental factors or geometric profiles. Conversely, collective cell groups can adapt their migratory actions based on interactions with neighbouring cells. Such constraints and behaviours can be represented through various components, including surface tension, active forces, elasticity, curvature, cell polarity, and pressure, among others [6].

Numerous quantitative models related to morphogenesis have been published, each targeting specific processes and contributing uniquely to our understanding of the multifaceted nature of morphogenetic events. Some models focus on the cell membrane as an infinitely thin, curved surface [7], enabling the study of filament alignment patterns. Others explore the influence of apical-basal and planar polarities on embryonic organisation [8]. Recent advancements include models that consider cell sheet deformation with curvature effects [9, 10], and those that use three-dimensional vertex models for *in vitro* organoids [11].

Despite these advances, gaps remain. For instance, the PhysiCell model [12] and the space-jump derivation for non-local models [13] lack comprehensive treatment of stochastic behaviour and open biological systems. Similarly, the DiVinE model checker [14] and the MONALISA software [15] have limitations in addressing cell-cell interactions and the dynamism of open biological systems,

* jesus.fuentes@uni.lu

respectively.

In this paper, we introduce a versatile model to unravel the role of geometry-constrained forces on tissue organisation and morphogenesis. The model integrates elastic and geometric forces, stochastic motion, and key cellular life events such as division and apoptosis. Our model can incorporate tissue or background geometry, representing the genetic information encoding for patterning and morphogenesis. This information is represented as geometrical forces driving the morphogenesis process and determining the final morphology of the system under study. However, the genetic information needs to be in line with the environmental state for the desired morphology to emerge. In our model the integration of parameters related to the state of the environment, allows us to capture shifts in cellular spatial distribution and morphology, changing the direction of the morphogenesis process. This adaptability captures the dynamics observed in pathological conditions, such as cancer development or embryonic malformations. Importantly, our model is comprehensive in its approach to simulating cell-cell interactions in dynamical open biological systems, capturing stochastic behaviour and accounting for genetic information driving the cells movement. This is crucial for capturing the natural heterogeneity and complexity of authentic tissue structures.

Furthermore, our model's ability to integrate tissue geometry enhances the fidelity of our simulations, bridging computational modelling with empirical research. This is particularly relevant for applications in tissue engineering, where geometric forces could serve as guiding or control forces for cellular configurations within scaffolds [16–18]. Looking forward, our model holds promise for simulating pathological scenarios, including oncology and regeneration studies.

In the forthcoming sections, the paper first delves into the mechanical and geometrical aspects of the model, elaborating on the forces that characterise it. This is followed by a rigorous examination of the intrinsic numerical error and the behaviour of our computational methods. Subsequently, we present a series of numerical simulations that scrutinise various parameters and hypothetical scenarios, thereby demonstrating the model's broad applicability across diverse geometries pertinent to biological systems. The final part of the paper is dedicated to a discussion on the model's robustness and the limitations of its capabilities.

II. MECHANICAL AND GEOMETRICAL MODEL

Our work aims to provide a comprehensive framework for simulating cell-cell interactions in dynamical open biological systems, capturing both deterministic and stochastic behaviours. The model is centred around a dynamic cellular system, where the total number of cells, denoted by N , may fluctuate over time due to

events like cell division and apoptosis. Each cell is symbolised by its centre of mass (COM), represented by the map $\mathbf{x}_i : t \mapsto (x_i(t), y_i(t), z_i(t))$ in \mathbb{R}^3 . This specific representation aims to maintain a close connection to real-world biological scenarios, wherein the interactions between cells as well as the influential role of the background play a significant part in shaping the overall motion of the cellular system.

To model the collective motion of cellular populations, we make use of the well-established Chandrasekhar's theory for molecular movements [19]. This theory, quite notably, helps to characterise each cell's evolution over time in adherence to the Langevin equation. In our model, we assume that the friction at play in the system is substantial enough to create over-damped conditions. This assumption essentially allows us to neglect the inertial term, which in turn reduces the equation of motion significantly. This simplified equation serves as the basis for our model, and is formulated as follows:

$$d\mathbf{x}_i = \mathbf{F}_i dt + \sigma_i d\mathbf{W}_i, \quad (1)$$

where the first term on the right-hand side constitutes deterministic forces while the second term symbolises individual stochastic forces for each cell. This equation of motion is presented in dimensionless variables; hence, all ensuing parameters will be without physical units. The stochastic force term is modelled as a Gaussian white noise with zero mean and a variance proportional to the infinitesimal increment dt , modulated by a diffusion coefficient σ_i . Besides, the stochastic force shall satisfy the fluctuation-dissipation theorem [20], $\langle \mathbf{W}_i(t) \cdot \mathbf{W}_i(t_0) \rangle \propto \delta(t - t_0)$, which ties the strength of random forces to the dissipation of energy in the system.

The effective force field experienced by each cell, \mathbf{F}_i , in (1) is represented by the linear superposition of components that mimic different interactions between cells and the medium:

$$\mathbf{F}_i = \sum_{j \in \mathcal{N}(i)} \underbrace{(\mathbf{F}_{ij}^e + \mathbf{F}_{ij}^v + \mathbf{F}_{ij}^r)}_{\text{interaction}} + \underbrace{\mathbf{F}_i^g + \mathbf{F}_i^N}_{\text{constriction}} \quad (2)$$

while the total force experienced by the entire cellular ensemble, is simply the summation of the individual force fields $\mathbf{F} = \sum_i^N \mathbf{F}_i$. The model architecture is presented in Figure 1. The terms within the summation in (2) account for pairwise interactions between the i th cell and its proximate neighbours j in $\mathcal{N}(i) \subset N$. Specifically, the force components in (1) encompass:

1. Deterministic Forces. These forces are essential for capturing the mechanical aspects of cellular interactions and movements. They are divided into interaction and constriction components, each serving a specific purpose:

- **Interaction Forces ($\mathbf{F}_{ij}^e, \mathbf{F}_{ij}^v, \mathbf{F}_{ij}^r$):** These forces model the elementary electrochemical interactions between cells. Elastic forces (\mathbf{F}_{ij}^e) mimic the natural tendency of cells to maintain a certain distance

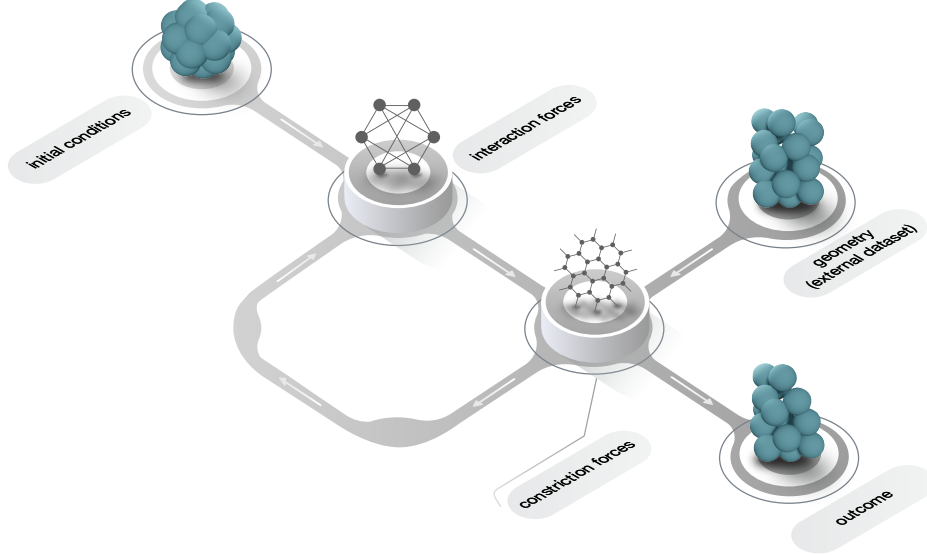


Figure 1. Schematic of the model architecture and its components. Interaction forces symbolise elementary interactions between cells, while constriction forces model the interactions that cells have with their surroundings. These constriction forces can be informed by external datasets.

from each other, akin to spring-like behaviour. Biophysically, these forces are essential for capturing the elastic properties of cells, which are influenced by the actin cortex and can undergo reversible deformations at small forces [21]. Viscosity-induced forces (\mathbf{F}_{ij}^v) account for the fluidic nature of the cellular environment, affecting the rate of cellular movement. At a biological level, viscous effects are significant at higher indentations and are influenced by the cellular response to the medium [21]. Repulsive forces (\mathbf{F}_{ij}^r) prevent cells from occupying the same space, simulating the effects of cellular membranes. They are crucial for capturing the long-range curvature forces in lipid-protein interactions that affect membrane shape transitions [22].

- **Constriction Forces ($\mathbf{F}_i^g, \mathbf{F}_i^N$):** Geometrical forces (\mathbf{F}_i^g) capture the influence of the underlying genetic information, including tissue or medium geometry, on cell movement. In biological systems, the geometry is contained in the genetic code and can significantly influence cellular functions, such as migration and differentiation [9, 23]. Moreover, these forces can be particularly useful in tissue engineering and scaffold design, where control over cellular orientation and placement is crucial. By manipulating the Gaussian curvature, one can guide cells into specific configurations to capture the geometry of biological tissues. The neighbouring correction pseudo-forces (\mathbf{F}_i^N) adjust the forces based on local density variations, ensuring a more realistic simulation of tissue dynamics. They

are motivated by the need to capture the mechanical linkage between different cellular components, such as regulatory and catalytic subunits in protein complexes [24].

2. Stochastic Forces. These forces introduce randomness into the model, capturing the inherent variability and adaptability of biological tissues. They are modelled as Gaussian white noise, satisfying the fluctuation-dissipation theorem, which ties the strength of random forces to the dissipation of energy in the system.

A thorough examination of each force component is provided in the following subsections.

A. Cell interaction forces

To discuss the role of interaction forces, we first direct our attention towards the elasticity term, given as:

$$\mathbf{F}_{ij}^e = -k_{ij}(\|\mathbf{x}_i - \mathbf{x}_j\| - l_0) \frac{\mathbf{x}_i - \mathbf{x}_j}{\|\mathbf{x}_i - \mathbf{x}_j\|}, \quad (3)$$

which, in the landscape of forces, gains particular prominence due to its mimicry of the behaviour of a Hookean force—a widely recognised model for particles that are interconnected by elastic bonds. The parameters k_{ij} and l_0 represent the spring constant and the rest length, respectively. Deviations from this rest length, which are largely dictated by the specific type of cells, instigate restorative forces between the particles, thus simulating an elastic behaviour. It is essential to note that, as per Newton's third law, this force is pairwise, acting along the line directly connecting the two cells. This force aims

to return the distance between them to the equilibrium distance, denoted by l_0 , hence eliciting an equal and opposite reaction on the two cells. The result of this action is a tendency to compress the cells when they are too far apart and extend them when they are too close together.

The model, in addition to accommodating the elastic forces, also incorporates damping or viscosity-induced effects through:

$$\mathbf{F}_{ij}^v = -\eta_{ij} \frac{d}{dt}(\mathbf{x}_i - \mathbf{x}_j). \quad (4)$$

In this context, η_{ij} are the damping coefficients that modulate the degree of resistance the environment imposes on motion. The damping force bears proportionality to the relative velocity of the cells. It is important to remark that for the calculation of the damping force, we need to take into account the relative velocity of the cells. This requires that the damping force term takes into consideration the difference in the displacement of the two cells from previous time to the current one.

The final constituent of the interaction forces is the repulsion force. This is delineated in the equation:

$$\mathbf{F}_{ij}^r = a_{ij} \frac{\mathbf{x}_i - \mathbf{x}_j}{\|\mathbf{x}_i - \mathbf{x}_j\|^3}. \quad (5)$$

This term is responsible in modelling the repulsion that arises when cells encroach too closely on each other, with a_{ij} denoting the coefficients of repulsion. Similar to the other interaction forces, this force asserts itself along the line uniting the two cells, and always exerts a repulsive effect, striving to push the cells apart. Simultaneously, the force is modulated by (3) to prevent the cells from being ousted from the simulation domain.

Even more, the three cell interaction terms (3)-(5) reflect the flexibility of our model in simulating non-homogeneous scenarios within the cell population. By permitting different strengths for each cell-cell interaction (k_{ij} , η_{ij} , and a_{ij}), the model embodies a relaxed approach to cell mechanics. The intertwining of these parameters embodies the global behaviour of the cells, thereby necessitating their careful selection in accordance with the empirical specifics of the biological scenario under examination.

B. Constriction forces

Our model incorporates constriction forces, which not only restrict the interaction forces to predefined configurations, but also set the stage for directed cell movement. This aspect of our model is crucial in approximating the complex interaction between genetic information and environment within which biological cells function and manoeuvre. It establishes a connection between cellular information, behaviour and the surrounding environment.

The complex interplay of cellular interactions and tissue's form of motion is simulated through forces evoked

by the geometric background, defined collectively as $\mathbf{F}_i^g = (\mathbf{F}_i^\rho + \mathbf{F}_i^s + \mathbf{F}_i^K)_i$. These fields, which we describe below, unite to regulate the spatial patterning of cells within the tissue structure, endowing the model with biologically realistic cellular behaviour.

In living organisms, cells exist within a three-dimensional space surrounded by neighbouring cells and the extracellular matrix. This spatial arrangement significantly influences cellular behaviour, including migration, proliferation, and interactions. These interactions result in driving forces that guide cells into a specific morphology genetically encoded. In our model, the surface term S , related to all previously defined geometric fields, serves as a representation of this microenvironment and the geometric structures that influence cellular behaviour.

The component \mathbf{F}_i^ρ , denotes the geometric force density. It is an attractive force pulling cells towards their nearest neighbour on the tissue surface S , formulated as:

$$\mathbf{F}_i^\rho = -b_i(1 + \rho(\mathbf{x}_i))(\mathbf{x}_i - \mathbf{S}_i^{\min}), \quad (6)$$

where \mathbf{S}_i^{\min} represents the point on the medium S closest to the cell at position \mathbf{x}_i . The Gaussian kernel density estimate at the cell's location is represented by $\rho(\mathbf{x}_i)$, and b_i are surface tension coefficients. By drawing cells towards their closest point on S , it reflects the natural tendency of cells to align or cluster with neighbouring cells, motivating a distribution mirroring the tissue structure. Concurrently, the kernel ρ serves to repel cells from congested regions over S , thereby promoting a more uniform cell distribution.

In contrast to the force density which distributes itself uniformly across the surface, we introduce another component that guides the movement of the cell towards the medium. This directional approach aims to ensure that cells maintain a consistent path from their initial position towards the tissue surface. This force, represented by \mathbf{F}_i^s , is oriented towards a point on S that aligns with the cell's original direction from the centre of a unit sphere—the initial spatial distribution. Given the cell's position \mathbf{x}_i , its direction from the centre of the sphere is determined by the unit vector $\mathbf{d}_i = \mathbf{x}_i/\|\mathbf{x}_i\|$.

Because each point on the surface S has a direction from the centre of the initial condition, for a point S_k , where k indexes over the points of S , its direction is given by $\mathbf{s}_k = S_k/\|S_k\|$. Hence, the point on S that aligns with the direction of the cell \mathbf{d}_i is identified by the inner product of \mathbf{d}_i with every \mathbf{s}_k . Therefore, the point $\mathbf{S}_i^{\text{dir}}$ on S corresponding to the highest inner product value is the desired point, expressed as $\mathbf{S}_i^{\text{dir}} = \text{argmax}_k(\mathbf{d}_i \cdot \mathbf{s}_k)$.

With $\mathbf{S}_i^{\text{dir}}$ identified, the force \mathbf{F}_i^s pushing the cell \mathbf{x}_i towards $\mathbf{S}_i^{\text{dir}}$, is given by:

$$\mathbf{F}_i^s = -c_i(\mathbf{x}_i - \mathbf{S}_i^{\text{dir}}), \quad (7)$$

where c_i is the strength of the surface tension. This methodology ensures that the cell moves towards a point on the tissue surface that preserves its original departure

direction from the initial position. The concept of *directional guidance* has been leveraged in various other models [25, 26].

Modelling dynamical interactions of cells with their medium requires consideration of not only geometric constraints but also intrinsic surface properties like curvature. Curvature inherently impacts how cells perceive and navigate their surroundings. During embryonic development, there are a number of different evolutionarily conserved rearrangements, which result from alterations in shape and, consequently, lead individual cells to rearrange with respect to each other [27]. We then introduce the mean curvature force, $\mathbf{F}_i^{\mathcal{K}}$, offering a straightforward yet potent way to incorporate curvature effects:

$$\mathbf{F}_i^{\mathcal{K}} = -h_i \mathcal{K}_i \mathbf{n}_i. \quad (8)$$

In this expression, \mathcal{K}_i represents the mean curvature at the cell's position, and h_i quantifies the strength of the mean curvature force. To determine the curvature, we first identify a local neighbourhood within the surface S , based on a predefined neighbourhood size \mathcal{R} . The local neighbourhood, $S_{\mathcal{R}}$, is thus defined as the set of points in S that are closest to \mathbf{x}_i . Using this neighbourhood, we define an origin, \mathcal{O} , as the mean of the positions within $S_{\mathcal{R}}$. This process is reminiscent of transitioning from an affine to a vector space representation, where the affine space, devoid of a distinguished origin, encapsulates the relational structure between points, while the inclusion of \mathcal{O} establishes a local vector space.

The local coordinates of points in $S_{\mathcal{R}}$ are then computed relative to \mathcal{O} , allowing us to form a covariance matrix, \mathbf{C} , of these local coordinates. The eigenvector associated with the smallest eigenvalue of \mathbf{C} , yields the normal direction at \mathbf{x}_i , denoted \mathbf{n}_i .

To compute the mean curvature \mathcal{K}_i , we employ the local coordinates and the normal vector as:

$$\mathcal{K}_i = \frac{1}{\mathcal{R}} \sum_k^{\mathcal{R}} (\mathbf{L}_k \cdot \mathbf{n}_i)^2, \quad (9)$$

where \mathbf{L}_k are the local coordinates in $S_{\mathcal{R}}$. Curvature-based forces have wide applications, ranging from surface tension in fluid dynamics to elasticity in solid mechanics [28–31]. In our model, it aids in regulating cell adhesion and migration, offering biological plausibility.

The background-induced forces (6)-(8) together exert a persuasive effect on each cell, capturing the genetic and environmental constraints and ensuring the cells remain within the boundaries of the tissue or background structure. It offers a geometrical method to control the spatial positioning of cells in relation to a defined surface S . Overall, the whole field \mathbf{F}_i^g serves as a guiding principle, nudging the cell towards a previously defined surface and ensuring its confinement within the tissue structure.

A promising application of the component \mathbf{F}_i^g lies in its potential derivation from empirical data, such as point clouds generated from imaging techniques like magnetic resonance imaging or computerised tomography scans of

actual tissues [32]. These point clouds could subsequently be transmuted into a three-dimensional surface employing techniques like triangulation or parametric surface fitting [33]. This strategy would empower our model to capture the natural heterogeneity and complexity of authentic tissue structures.

The inclusion of the surface tension coefficients b_i, c_i, h_i also introduce a measure of adaptability in the model. By varying these parameters, not necessarily uniformly for every cell, we can simulate differing degrees of cell affinity towards the tissue surface, accounting for potential differences in cell adhesion characteristics. For instance, lower values in this set of parameters could represent cells with a low propensity to adhere to the tissue surface. This could be particularly useful when modelling scenarios such as the movement of cancerous cells, which often exhibit divergent adhesion characteristics compared to their healthy counterparts, enabling their invasive and metastatic tendencies [34].

Further expanding the model, we introduce another constriction term, tactically designed to implement a penalty force for those cells that settle into positions with a neighbour count which is either excessively high or dramatically low compared to their counterparts within the ensemble. This feat is accomplished by the integration of a neighbourhood term, mathematically represented as follows:

$$\mathbf{F}_i^N = -\alpha_i \text{sign}(A^{\text{opt}} - |\mathcal{N}(i)|)(\mathbf{x}_i - \mathbf{x}'_i), \quad (10)$$

herein, \mathbf{x}'_i stands for the location of cell i at the preceding time t' , such that $t > t'$. The constriction force encapsulates the penalties α_i , levied as punitive measures for any deviations $|\mathcal{N}(i)|$ from a targeted degree of cell connectivity A^{opt} , commonly understood as the number of neighbours. Therefore, this term influences the ensemble of cells by regulating the spatial uniformity of their distribution, thereby subtly guiding the cells towards sustaining their favoured configurations. Our suite of simulations adheres to the parameters $A^{\text{opt}} = 5$, $\alpha_i \sim 1 \times 10^{-4}$ across the entire spectrum of i indices. As for the neighbours \mathcal{N} , their computation is detailed in the next section.

C. Modelling open systems

In the network of cell-cell interactions, a key step towards accurate modelling involves correctly identifying neighbouring cells. Traditionally, there are several strategies for approximating these nearest neighbours [35–37]. Techniques such as a k-Nearest Neighbours method or the deployment of a k-d tree structure have been utilised in different works in the literature [38–40]. However, our current methodology revolves around the introduction of a threshold distance l_T , which serves to delineate the extent of interaction forces, thereby refining the demarcation of neighbours.

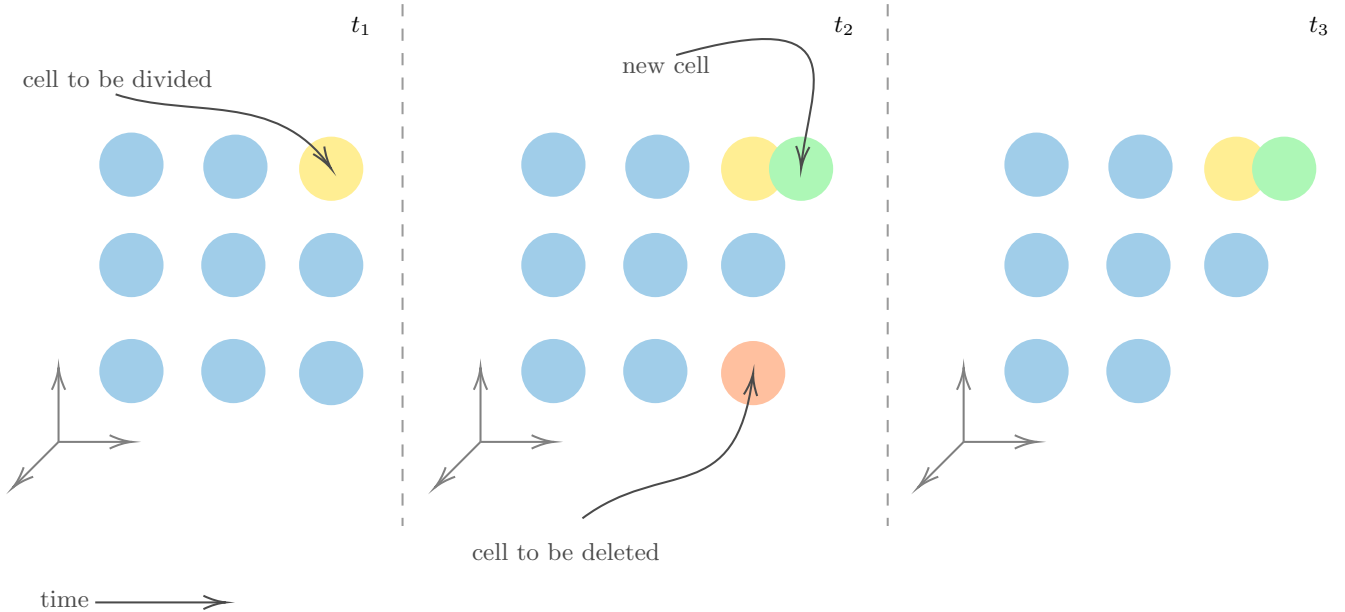


Figure 2. Schematic illustration of the model’s cell event timeline. Starting from an initial cell configuration, events like division or death are scheduled. For instance, if a cell is set to divide at time t_1 , a new cell will emerge at t_2 . Conversely, if a cell is scheduled to die at t_2 , it will vanish by t_3 . This sequence dictates the evolving morphology of the cellular ensemble.

The threshold distance l_T is calculated according to the formula:

$$l_T = \frac{2}{N(N-1)} \sum_{i=1}^N \sum_{j=i+1}^N \|\mathbf{x}_i - \mathbf{x}_j\|, \quad (11)$$

where N represents the total number of cells at time t and \mathbf{x}_i and \mathbf{x}_j are the positions of cells i and j respectively. With this threshold established, the neighbours of the i -th cell are defined as the set of cells j that fall within the threshold distance l_T from the i -th cell. This is expressed as:

$$\mathcal{N}(i) = \{j \mid 1 \leq j \leq N, j \neq i, \|\mathbf{x}_i - \mathbf{x}_j\| \leq l_T\}. \quad (12)$$

A key feature of our model is that it seeks to capture the dynamism of biological systems, accounting for temporal changes induced by events such as cell division and apoptosis. As time evolves, the system state \mathbf{x} is updated to capture these events. These events are randomly distributed over a given interval of the simulation time, and limited to a predetermined number of occurrences.

To illustrate this, consider a discrete time horizon for our simulation given by:

$$\tau = t_0, t_1, \dots, t_{N_{\text{steps}}}.$$

For any given simulation run, the number of division events is symbolised by D and the number of apoptosis (or death) events by A , such that $N_{\text{steps}} \geq A + D$.

To provide structure to this dynamism, we introduce a function ϕ , which maps a given timestep in τ to a cellular event in the set E . The set E consists of tuples, where

each tuple contains a time step and its associated cellular event. Formally:

$$E = \{\{t_k, \text{event}_k\} \mid t_k \in \tau, \text{event}_k \in \{\text{division}, \text{death}\}\},$$

where k ranges from 0 to $A + D$. Given the aforementioned definition, the function ϕ maps a time step (t_k) to a tuple (t_k, event_k) . These events are then randomly distributed across the simulation horizon τ . Figure 2 provides a schematic illustrating how this process is scheduled.

If no divisions or deaths are set to occur (i.e., the simulation is to maintain a constant number of cells), then $D = A = 0$ and therefore ϕ yields an empty set $E = \emptyset$. Otherwise, the number of cells within the ensemble will vary according to the number of division and death events.

In the process of cell division, a particular cell \mathbf{x}_i in the ensemble is randomly selected to undergo division. The position of the new cell is determined by adding a small displacement vector, $\delta \in \mathbb{R}^3$, to the mother cell \mathbf{x}_i . The small vector δ is drawn from a standard normal distribution with standard deviation set to a determined value. This new cell position is then added to the system, as:

$$\mathbf{x}' = \mathbf{x} \cup \{\mathbf{x}_i + \delta\}. \quad (13)$$

On the other hand, for cell death, a cell is randomly selected for removal. This results in a new system state where the selected cell has been eliminated, expressed as:

$$\mathbf{x}' = \mathbf{x} \setminus \{\mathbf{x}_i\}. \quad (14)$$

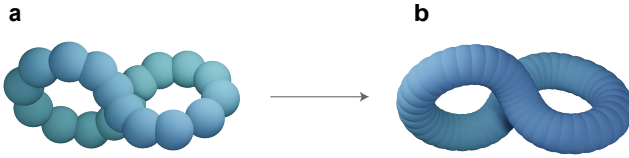


Figure 3. Panel **a** displays a group of 20 cells distributed over certain geometry. Panel **b** illustrates the same arrangement of cells after two rounds of cell division in each cell. It is important to note that during this process, the intrinsic curvature is largely maintained while there is a slight increase in volume. This diagram depicts the process of cell division in our model, where cellular structures within an organism or tissue undergo expansion and replication as illustrated in Figure 2.

Refer to Figure 3 for a visualisation of the division process in our model. In it, Panel a shows an initial arrangement of cells, and Panel b represents the aftermath of two division rounds for each cell. Our model's design, rooted in open systems modelling, aptly captures the stochastic nature of cell-cell interactions. Over time, the system undergoes continuous evolution, primarily driven by the probabilistic events of cell division and apoptosis. Within our code, we detail the algorithm that identifies the nearest neighbours, using cell positions and a specified threshold distance, l_T .

D. Code availability

Our code, written in Python, is openly accessible to the general public. It can be found, alongside its documentation, at github.com/fuentesigma/pygen.

III. NUMERICAL TESTS AND ERROR ANALYSIS

To ensure the reliability of our numerical solutions, we conducted a series of tests centred on both the behaviour of the model under specific conditions and the associated numerical errors.

In addressing the equation of motion (1), we employed the Euler-Murayama method, an efficient numerical scheme for stochastic differential equations subject to known initial conditions:

$$\mathbf{x}_i(t + dt) = \mathbf{x}_i(t) + \mathbf{F}_i(t) dt + \sigma_i d\mathbf{W}_i(dt), \quad (15)$$

where dt represents a small increment of time at which the system evolves in each step. From now on, in all simulations, we opted for $dt = 1 \times 10^{-3}$ to blend computational efficiency with numerical precision. Our chosen value for the stochastic strength, $\sigma = 1 \times 10^{-3}$, mirrors scenarios where stochastic forces are subtle yet present.

For the first test, we modelled the system with a fixed counting of $N = 20$ cells, uniformly spread across a unit sphere at initial time. Cell behaviour was predominantly influenced by constriction forces, (6)-(8), shaped by the geometry S of the cylinder, mimicking tubular structures found *in vivo*:

$$\mathbf{r} = \begin{pmatrix} \cos(\theta) \\ \sin(\theta) \\ z \end{pmatrix}, \quad \theta \in [0, 2\pi], \quad z \in [-1, 1]. \quad (16)$$

All cells shared common parameters for elasticity, viscosity, and repulsion forces, with their values set at 1×10^{-2} . Moreover, surface tension coefficients were consistently homogeneous across cells. We gauged our method's accuracy by computing the root mean square error for solutions \mathbf{x} at time $T = 1$, with time steps spanning from 10^{-6} to 10^{-1} . The results of these calculations are presented in Figure 4.

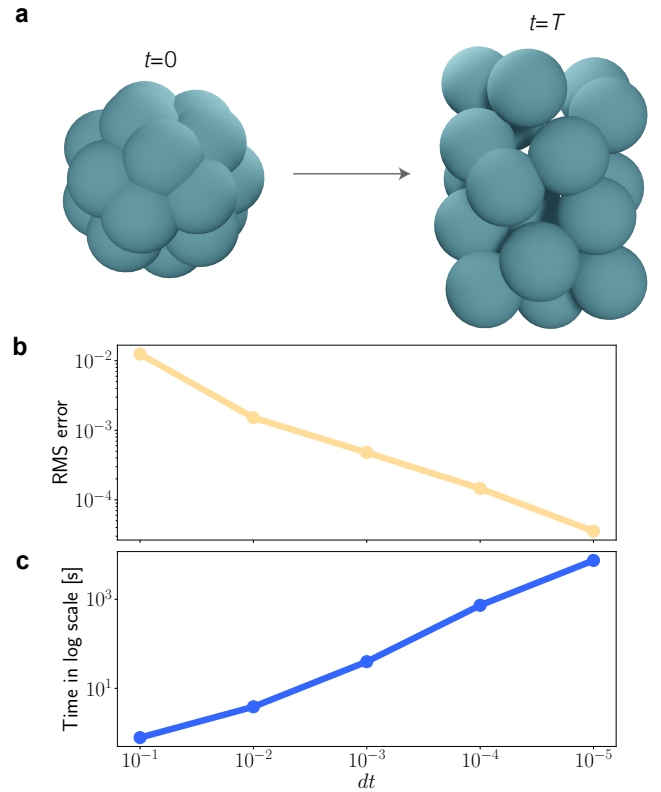


Figure 4. Numerical error assessment. Panel **a** showcases the model's transition from a spherical to a cylindrical configuration using different increments dt . Panel **b** contrasts the error of solutions derived at different time steps against a reference solution at $dt = 1 \times 10^{-6}$. Panel **c** illustrates the computation duration associated with each simulation across different time steps, this highlights the reasonable balance between numerical error and computational resources achieved at our selected time step of 10^{-3} .

In the second test, we evaluated the consistency of volume during cell division. Beginning with 50 cells uniformly distributed on a sphere with a radius of $1/2$, the

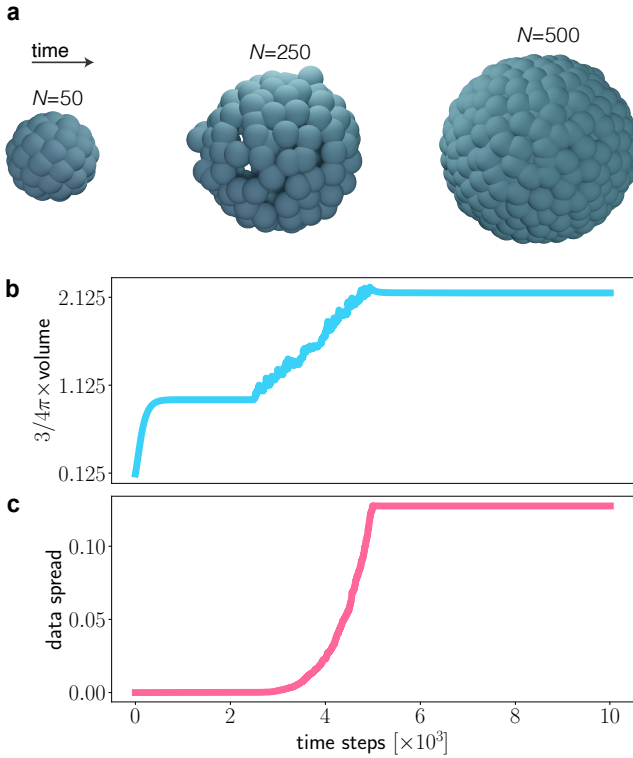


Figure 5. Analysis of cellular division and model accuracy. Panel **a** illustrates the cell division from an initial 50 to a final count of 500 cells. Panel **b** depicts the volumetric dynamics throughout the simulation, indicating stationary state after the 5×10^3 time step mark. Panel **c** portrays cell distribution over the sphere's surface as quantified by the determinant of the covariance matrix across time intervals.

simulation was governed by constriction forces defined by a unit sphere's geometry. The cell count expanded nine-fold, leading to 450 new cells by the end of the simulation, as shown in Figure 5. Completing 1×10^4 time steps, the total cell count rose to 500. The final distribution of the cell population closely conformed to a sphere with a radius $r \approx 5/4$. The ultimate spatial arrangement of the cell population around the intended geometry is influenced by the chosen intercellular distance l_0 in (3).

In our morphogenesis simulation, for the initial 2.5×10^3 time steps, we deliberately set the cell population to evolve without any division or death events. During this phase, the volume of the cellular configuration grew until it roughly equated the volume of a unit sphere. This growth is illustrated in panel b of Figure 5, where the volume progression reaches a consistent plateau. Following this phase, under the cellular events E , we allowed cells to undergo divisions, each one producing up to 9 new cells while prohibiting cellular death. This proliferation continued until the 5×10^3 time step mark. From this point onward, the volume of the sphere remained constant for the duration of the simulation.

The spatial distribution of cells throughout the simulation is visualised in panel c of Figure 5. To quantitatively analyse the spread of cell distribution over different time steps, we computed it as the determinant of the covariance matrix of the cells. This data reveals how cells transition from their initial state to positions governed by constriction forces, ensuring they remain within the boundaries of the biological system, S . However, with the cell-cell equilibrium distance parameter set at $l_0 = 1$, not all cells perfectly aligned on the sphere's surface; some were positioned slightly below their neighbours along the boundary.

IV. TESTING THE MODEL FOR SYNTHETIC MORPHOLOGIES

In this section, we aim to demonstrate the extensive applicability and versatility of our model by showcasing a variety of simulations across different geometries. Our main objective is to present proof-of-concept morphologies that exemplify the model's ability to guide a set of cells towards a target geometry. Although these simulations are not confined to any specific biological system, they remain relevant to a wide range of living organisms. Our model is capable of reconstructing the dynamics between initial and final morphology states, each defined geometrically, making it applicable across a diverse range of biological systems.

We explore tubular structures as well as knot-like topologies, vital in biological contexts. Tubular structures, ubiquitous in biology, are essential for functions ranging from vascular transport in animals to nutrient absorption in plants. They demonstrate remarkable resilience and adaptability, factors our model aims to capture. In the macroscopic realm, the intertwined growth patterns of certain plants and vines exhibit knot-like geometries, evolved for robustness against environmental challenges. The *Clathrus ruber*, or lattice stinkhorn, exemplifies knot-like morphogenesis. It transforms from an initial 'witch's egg' state into a mature, lattice-like structure, a three-dimensional nth-foil form akin to interlaced knots. This presents an ideal case to test our model's ability to replicate complex biological geometries [41].

This section will survey three specific simulation scenarios: the morphogenesis of a simple twisted tubular structure, the deformation and subsequent evolution of a complex foil knot, and a tissue regeneration process. The first scenario, involving a simple deformed cylinder, offers a foundational understanding of our model's capabilities in representing tubular structures. Subsequently, we challenge our model by deforming knots, adding a layer of complexity to the geometry and analysing how this influences the resulting cell organisation. Lastly, we survey a tissue regeneration scenario, investigating how our model copes with dynamic changes in cell populations and geometry.

A. Tubular Structures

The simulation of morphogenesis below focuses on the dynamics of constriction forces within the framework of tubular structures. Such structures are emblematic of numerous biological systems, where tubular formations play a critical role in morphological and functional aspects, from vascular networks to organ development.

The simulation commences with a set cell population of 200, carefully balanced to negate any fluctuations due to cell division or death. This constancy is crucial for the analysis of morphogenesis independent of cellular population dynamics—which we will discuss later.

The initial conditions are defined by a uniform spatial distribution of cells across a unit sphere. This baseline state is visually expounded in Figure 6, which showcases the evolution of three stages across 1000 time steps. The sequence, displayed from left to right, illustrates the transformation from an earlier state to a hollow, twisted tubular structure—typically found in the intestines, stems in plants, or the vascular systems of animals and plants, where they function as conduits for blood and nutrients.

Central to our simulation is the geometry S , a primary determinant of the constriction forces. The geometry of the structure is articulated through a position vector $\mathbf{r} = (x, y, z)$, where x and y are the coordinates in the plane, and z is the height. These coordinates are generated through a computational mesh. Specifically, the azimuthal angle θ and the vertical coordinate z are varied linearly, creating a grid. Upon this grid, the coordinates of a cylindrical structure are initially computed. Then, a sinusoidal deformation is applied, modifying the original cylinder into a twisted tubular form.

The parameters governing the simulation are chosen to mirror the dynamics of biological cell interactions. The cell-cell equilibrium distance, denoted as l_0 , is set to 1×10^{-2} , reflecting a scenario where cells are close to each other. The adhesion (k) and repulsion (a) coefficients, both fixed at 1×10^{-2} , emulate the balance of forces that govern cellular assembly and structure. The cell-tissue surface tension parameter, γ , is assigned a value of 1.0, indicative of a predominant role of the geometric forces in comparison to the interaction forces.

Further, the simulation incorporates fixed parameters crucial for its temporal and spatial fidelity. The diffusion coefficient (D), set at 1×10^{-3} , encapsulates the random motion inherent in cellular systems. The time step (dt) and cell-fluid friction (η) are calibrated at 1×10^{-3} and 1×10^{-4} , respectively, for all cells.

The constriction forces, crucial for shaping the tubular structure, are uniformly parameterised. The strengths of these forces, denoted by b_i, c_i , and h_i , are set to unity for each cell. This uniform application of forces is instrumental in examining the morphological changes driven primarily by the tubular geometry.

B. Deformed Knot-like Structures

The next proof-of-concept suite of simulations incorporates constriction forces guided by a hypothetical morphology of a single-parameter foil knot—a form of torus knot manifesting on the surface of a torus in three dimensions. To frame this discussion with rigour, we first establish the relevant topological and geometric contexts.

In our study, the three-dimensional Euclidean space, \mathbb{R}^3 , is the canvas whereon the foil knot emerges as a subset. It is construed as an embedded one-dimensional sub-manifold within \mathbb{R}^3 , endowing the foil knot with local properties akin to those of the Euclidean space \mathbb{R} .

Typically, torus knots are characterised by two integer parameters specifying the number of times the knot traverses the internal circular path of the torus and loops around its rotational symmetry axis. However, we take a different approach for our simulation by employing a single parameter, θ , to define the foil knot residing on a torus.

Herein, the azimuthal angle θ engenders a foil knot, whose position vector $\mathbf{r} = (x, y, z)$ is articulated thus:

$$\mathbf{r} = \begin{pmatrix} \cos(n\theta) \cos(\theta) \\ \cos(n\theta) \sin(\theta) \\ \sin(n\theta) \end{pmatrix}. \quad (17)$$

This formulation of \mathbf{r} transmutes the interval $[0, 2\pi]$ into \mathbb{R}^3 , thereby morphing a simple circle into an n -lobed foil knot.

In the domain of knot theory, this manifestation aligns with an $(n, 1)$ torus knot, where n is a topological invariant, pivotal in determining the knot's lobes and thus its complexity. Our specific case showcases a rich structure as θ varies, paving the way for probing diverse proof-of-concept biological structures.

We explored the effects of topology alteration in the foil knot by setting $n = 2$, thereby complicating its form through external deformations applied to the y and z axes. These deformations, quantified in the Cartesian coordinates, transform the knot as follows:

$$\mathbf{r} = \begin{pmatrix} \cos(n\theta) \cos(\theta) \\ \cos(n\theta) \sin(\theta) + \delta \cos(\theta) \\ \sin(n\theta) + \delta \sin(2\theta) \end{pmatrix},$$

where δ denotes the deformation parameter, θ is the angular parameter. Here, $\delta = -1/2$ is posited, illustrating an augmentation in the knot's geometry and, consequently, in the spatial arrangement of cellular structures.

Morphogenesis simulations of these deformed configurations, as depicted in Figure 7, commence with 250 cells arrayed over a unit sphere. Over 5000 time steps, the cell population dynamically evolves under cellular events managed to introduce 250 new cells through cell division while gradually eliminating 50 cells, thereby resulting in a final cell count of 450. This flow underlines the morphological evolution within the deformed topological confines of the foil knot.

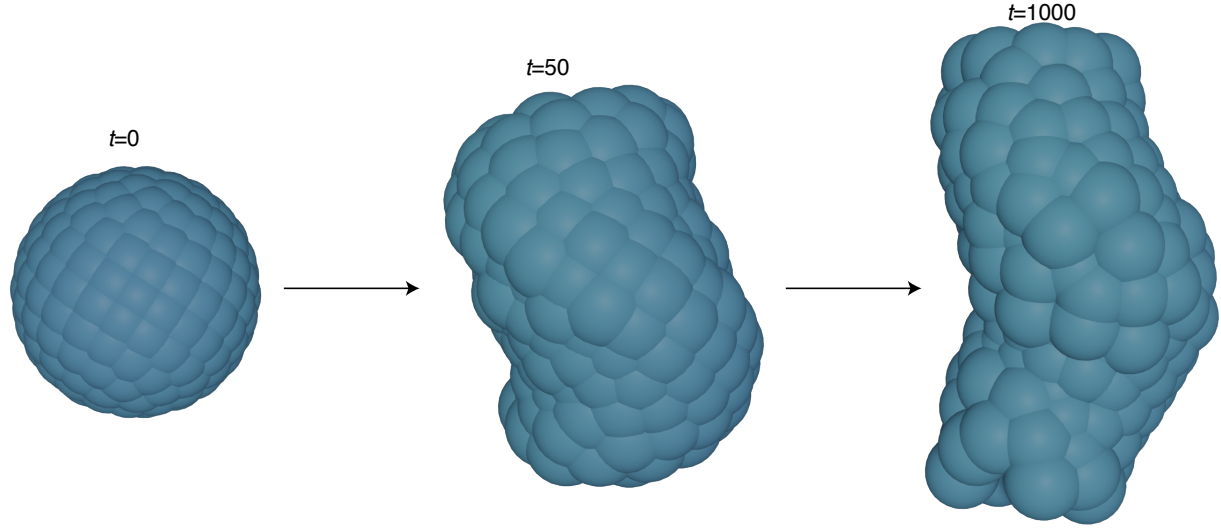


Figure 6. Twisted Tubular Structures in Simulated Morphogenesis: This figure delineates the progressive stages of morphogenesis as simulated within our model, focusing on the development of a twisted tubular structure. The depicted stages are at three critical junctures: $t = 0$, $t = 50$, and $t = 1000$ in simulation steps, beginning from a unit sphere as initial condition. The evolution is displayed from a stage close to the nascent form, following by an intermediary stage depicting significant structural development, and the final stage at $t = 1000$ vividly illustrating the model’s capacity to guide cellular configuration to a defined geometry. This outcome contrasts with prevalent self-assembly models in morphogenesis, proving our model’s geometry-driven approach. It demonstrates that, under specific conditions, an initial cellular arrangement can be methodically directed towards a predetermined structural configuration, highlighting the potential of guided morphogenesis in understanding and replicating complex biological structures.

In Panel a of Figure 7, we hold the cell elasticity coefficients fixed to 1×10^{-2} , indicative of homogeneous adhesion across all cells. This constraint ensures uniformity in the morphological dynamics of the cells. The cell-cell equilibrium distance l_0 was maintained at 1×10^{-1} . The scenario also assumes an almost negligible cell-fluid friction, with coefficients η_{ij} in the order of 1×10^{-4} . To counterbalance the attraction forces, we fixed the repulsion force strengths $a_{ij} = 1 \times 10^{-2}$. Meanwhile, the strengths of the constriction forces b_i, c_i and h_i were fixed to unity for every i .

In contrast, Panel b introduces a layer of stochasticity by assigning the cell elasticity coefficients as uniformly distributed random numbers between 0 and 1, thereby invoking inhomogeneous adhesion across the cell population. This allows us to study the interplay between the structurally complex, geometrically altered foil knot, the dynamic changes in cell count, and the varying mechanical properties of the cells themselves. As in Panel a, the rest of the parameters remain as in the previous set of simulations.

Our exploration into these two scenarios serves as a proof-of-concept of the capacity of our model to represent the morphogenetic outcomes that emerge from the topological complexity, inherent in the deformed foil knot and the mechanical heterogeneity within the cell population. As an illustration, Panel a and b documents the temporal evolution of volume within each scenario. Observing the homogeneous case illustrated in Panel a, we find it leads

to a smaller volume compared to the inhomogeneous scenario depicted in Panel b. This distinction reflects the significance of cell-cell adhesion in shaping morphogenesis. A homogeneous adhesion profile often assures well-regulated structure formation, preserving the geometry-dictated form. Conversely, the presence of stochastic variations in cell-cell adhesion can give rise to irregularities in tissue formation, with the overall geometry being less faithfully reproduced.

C. Tissue Regeneration

A remarkable ability observed in certain biological systems is the capacity for tissue regeneration. An array of living organisms, from simple unicellular entities like bacteria to complex multicellular systems like starfish, display the incredible phenomenon of regenerating their damaged tissues and organs. This regenerative process often involves a puzzling interplay between cell proliferation, migration, and differentiation, guided by a combination of intrinsic cellular machinery and external chemical cues.

In our investigation, we seek to understand the underlying morphogenetic dynamics of tissue regeneration through the framework of topological constraints and cell mechanical properties. We construct this exploration around a foil knot with $n = 2$, as presented in the previous section. The simulation parameters are predom-

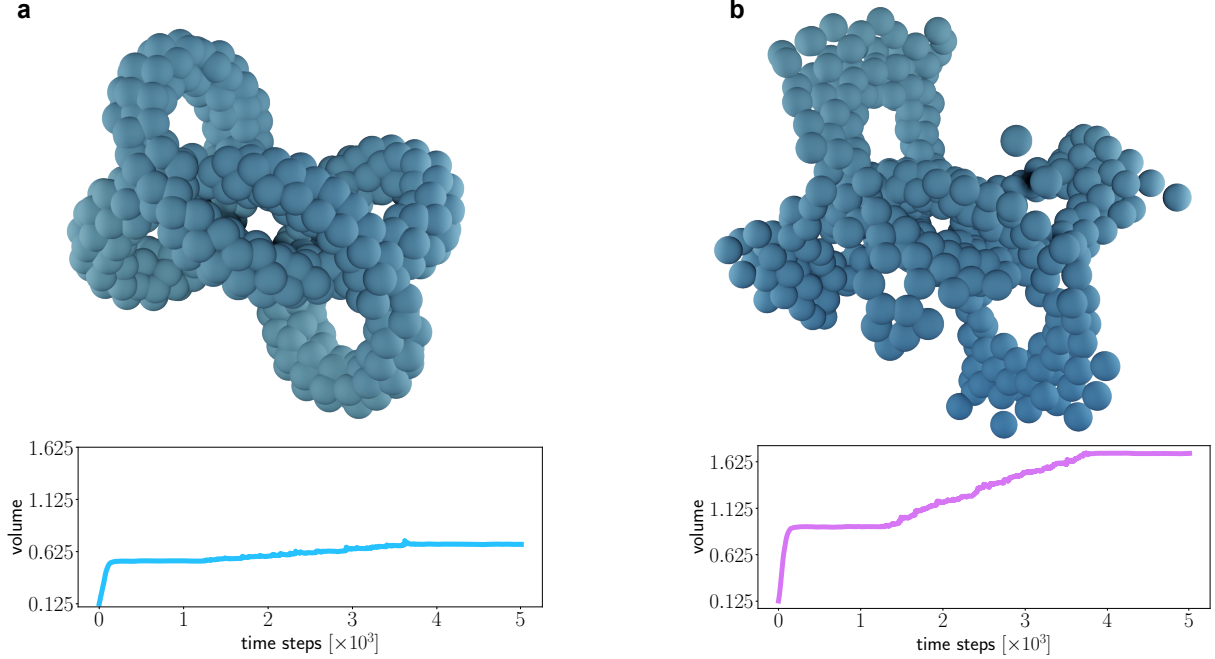


Figure 7. Deformed foil knot simulations under distinct cellular conditions. Panel **a**: Morphogenesis of 250 cells over 5000 steps, resulting in 450 cells due to division and apoptosis. All cells have a uniform elasticity coefficient of 1×10^{-2} , showcasing the outcome of homogeneous adhesion. Panel **b**: Morphogenesis with elasticity coefficients for each cell varying between 0 and 1, revealing effects of heterogeneous adhesion. Accompanying plots show the temporal evolution of volume, illustrating the impact of adhesion variability on structure formation.

inantly preserved from the scenario in Figure 7a, with a distinct alteration to the simulation timeline. We initially allow the system to evolve for 7000 time steps, during which the system dynamically transitions from an initial spherical distribution of 500 cells to the geometry of the foil knot $n = 2$. This transformation is facilitated by the inherent topological constraints and cell mechanical interactions, following the blueprint embedded in the foil knot structure.

After reaching the 7000-time-step mark, we intentionally disrupted the evolved structure by removing a proportion of cells, as shown in Figure 8. For a visual representation of this process, we refer readers to the supplemental videos accompanying this paper. This artificial manipulation mirrors the physiological disruptions that a biological tissue might experience due to injury or disease, leading to a loss of tissue volume and an alteration in tissue structure. Notably, this cell removal process results in a significant modification to the tissue topology, transforming it from the foil knot structure into a less regular form.

To initiate the regenerative process, we then prescribe 100 new cells to be produced, while concurrently inducing apoptosis in a distinct set of 50 cells. The system then progresses over a subsequent 3000 time steps, allowing us to observe the reconstruction of the original topology. The regeneration of the foil knot structure is not a trivial outcome. It demonstrates the remarkable resilience of

the cellular system in maintaining its original blueprint amidst the challenges of loss and reconstruction.

In essence, this simulation shows how our model is able to capture the dynamical and topological aspects of biological processes, such as tissue regeneration. It showcases how a cellular system can transit from a simple spherical structure to a complex knot, survive a substantial disruption, and then restore its original topology. Such a system offers a rich platform to understand the influence of geometric and topological constraints on tissue formation, disruption, and regeneration.

V. CONCLUSIONS

This study introduced a comprehensive model able to simulate cell-cell interactions subjected to geometrical constraints in open systems. The model captures both deterministic and stochastic elements, thereby offering a nuanced representation of cellular interactions and environmental influences, while appealing to realism.

The total effective force field within our model is a linear superposition of various components, each capturing different aspects of cell interactions and environmental influences. These forces are motivated by the need to capture the mechanical linkage between different cellular components and the inherent variability and adaptability of biological tissues [9, 21, 24].

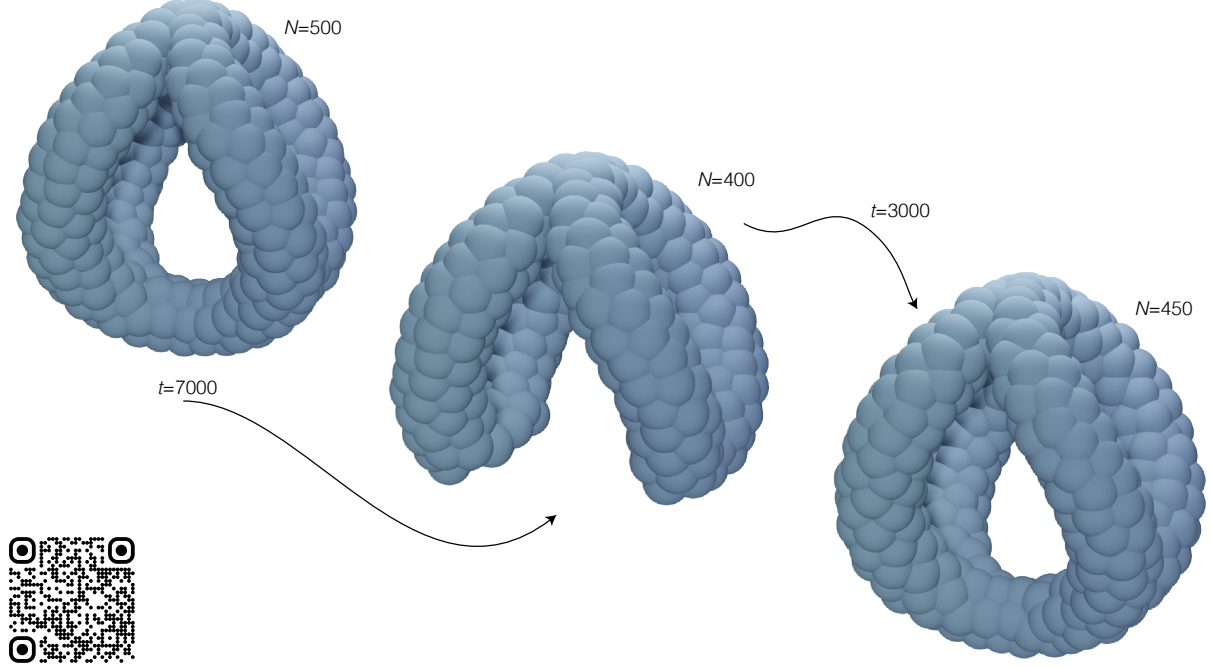


Figure 8. Tissue Regeneration in a Constrained Environment. Over 7,000 steps, we observe 500 cells coalesce into a foil knot of $n = 2$ complexity. Following an induced perturbation that leads to the removal of a cell cluster, an initially disrupted structure emerges. Remarkably, within the subsequent 3,000 steps, and through the introduction of 100 new cells coupled with apoptosis in 50 cells, the morphology undergoes a regenerative transformation. This process effectively demonstrates the inherent resilience of such systems in reinstating their original topology. For an interactive experience, readers are encouraged to scan the QR code located in the bottom left corner, which links to an augmented reality model of the depicted morphology.

A distinctive aspect of our model is its integration of geometric constriction forces, thereby creating a vital link between cellular behaviour and tissue architecture. This innovative feature is particularly relevant for applications in tissue engineering, where geometric forces could serve as guiding or control forces for cellular configurations within scaffolds [23].

Numerical simulations demonstrated the model's versatility in simulating diverse synthetic morphologies, reflecting the elasticity of cellular spatial dynamics within different tissue environments. The model's sensitivity to alterations in the background conditions was also highlighted, which can significantly influence cell behaviours and lead to unexpected tissue morphologies [42]. Therefore, an exciting prospect for future development of our model could involve incorporating cell proximity-based parameter values and probabilities for cell division and death, allowing for simulation of the unique characteristics of cells in pathogenic environments.

Beyond its applications in standard physiological conditions, our model's adaptability is particularly beneficial for simulating pathological scenarios. For instance, it could be employed to dissect the progression of diseases at the cellular level, thereby serving as a crucial instrument for hypothesis generation aimed at identifying therapeutic targets. This is especially pertinent in the field of oncology, where understanding the morpho-

genetic changes in cells is vital for describing the mechanisms of tumour growth and metastasis. The model's capability to simulate the dynamic interplay of forces and stochastic behaviour allows for a preliminary exploration of how cancer cells interact with their microenvironment, adapt, and evolve. Such insights contribute for developing targeted therapies and improving existing treatment strategies [43, 44].

From a biological perspective, these phenomena can be interpreted as the cell's adaptive response to environmental changes, triggering gene regulatory networks and metabolic cascades that shape tissue organisation. This is especially relevant for oncology, as cancerous cells often induce significant changes within host tissues to promote tumour growth and progression [42]. A unique feature of our model is its ability to incorporate external datasets representing tissue geometry—exemplified by the geometry S in the expressions (6)-(8)—, thereby bridging computational modelling and empirical research. This integration allows for a more accurate, context-specific understanding of cellular behaviour within actual biological systems, enhancing the relevance and applicability of our model across various biological fields.

Future work could expand upon this model by integrating more complex biochemical pathways and gene regulatory networks. This would enable analysis of the cellular responses at a molecular level, describing how cells

communicate and adapt within their microenvironments under both normal and pathological conditions. The potential to apply this model in predictive analytics for disease progression and treatment efficacy does also offer a promising avenue for clinical research. By simulating cellular behaviour in response to various therapeutic interventions, the model could assist in the development of personalised medicine approaches, tailoring treatments to the specific cellular and tissue characteristics of individual patients.

VI. ACKNOWLEDGMENTS

J.F. extends gratitude for the specialised technical assistance provided by Lupita Ruiz. Financial support for this research has been generously granted by the Fonds National de la Recherche, Luxembourg (FNR). Specifically, J.F. has been supported through the INTER/JPND/20/14609071 funding scheme, while M.M. has been funded under the PRIDE scheme (Grant No. 19/14063202/ACTIVE).

-
- [1] B. L. M. Hogan, Morphogenesis, *Cell Press* **96**, 225 (1999).
 - [2] C. Collinet and T. Lecuit, Programmed and self-organized flow of information during morphogenesis, *Nat Rev Mol Cell Biol* **22**, 245 (2021).
 - [3] S. Alt, P. Ganguly, G. Salbreux, and G. Salbreux, Vertex models: from cell mechanics to tissue morphogenesis, *Phil. Trans. R. Soc. B* **372**, 201502520 (2017).
 - [4] Z. Y. Liu, V. Trivedi, and I. Heemskerk, Mapping morphogenesis and mechanics in embryo models, *Nature Methods* **20**, 1859 (2023).
 - [5] D. A. Fletcher and R. D. Mullins, Cell mechanics and the cytoskeleton, *Nature* **463**, 485 (2010).
 - [6] K. Goodwin and C. M. Nelson, Mechanics of development, *Developmental Cell* **56(2)**, 240 (2021).
 - [7] J. R. Frank and M. Kardar, Trapped modes in acoustic waveguides, *Physical Review E - Statistical, Nonlinear, and Soft Matter Physics* **77(4)** (2008).
 - [8] B. Nissen, S. Ronhild, A. Trusina, and K. Sneppen, Defects in nematic membranes can buckle into pseudospheres, *eLife* **88**, 445 (2018).
 - [9] E. Hannezo, J. Prost, and J.-F. Joanny, Theory of epithelial sheet morphology in three dimensions, *Proceedings of the National Academy of Sciences* **111**, 27 (2014), <https://www.pnas.org/doi/pdf/10.1073/pnas.1312076111>.
 - [10] J. B. Kirkegaard, Curvature strains as a global orchestrator of morphogenesis, *Physical Review Research* **4(2)** (2022).
 - [11] T. Zhang and J. M. Schwarz, Topologically-protected interior for three-dimensional confluent cellular collectives, *Physical Review Research* **4**, 1 (2022).
 - [12] A. Ghaffarizadeh, R. Heiland, S. H. Friedman, S. M. Mumenthaler, and P. Macklin, Physicell: An open source physics-based cell simulator for 3-d multicellular systems, *PLOS Computational Biology* **14**, 1 (2018).
 - [13] A. Buttenschön, T. Hillen, A. Gerisch, and K. J. Painter, A space-jump derivation for non-local models of cell-cell adhesion and non-local chemotaxis, *Journal of Mathematical Biology* **76**, 429 (2018).
 - [14] J. Barnat, L. Brim, and D. Safránek, High-performance analysis of biological systems dynamics with the DiVinE model checker, *Briefings in Bioinformatics* **11**, 301 (2010), <https://academic.oup.com/bib/article-pdf/11/3/301/607245/bbp074.pdf>.
 - [15] P. Balazki, K. Lindauer, J. Einloft, J. Ackermann, and I. Koch, MONALISA for stochastic simulations of Petri net models of biochemical systems, *BMC Bioinformatics* **16**, 215 (2015).
 - [16] M. N. Collins, G. Ren, K. Young, S. Pina, R. L. Reis, and J. M. Oliveira, Scaffold fabrication technologies and structure/function properties in bone tissue engineering, *Advanced Functional Materials* **31**, 2010609 (2021), <https://onlinelibrary.wiley.com/doi/pdf/10.1002/adfm.202010609>.
 - [17] D. S. Sparks, F. M. Savi, C. E. Dlaska, S. Saifzadeh, G. Brierly, E. Ren, A. Cipitria, J. C. Reichert, M.-L. Wille, M. A. Schuetz, N. Ward, M. Wagels, and D. W. Hutmacher, Convergence of scaffold-guided bone regeneration principles and microvascular tissue transfer surgery, *Science Advances* **9**, eadd6071 (2023), <https://www.science.org/doi/pdf/10.1126/sciadv.add6071>.
 - [18] E. B. Peters, Endothelial progenitor cells for the vascularization of engineered tissues, *Tissue Engineering Part B: Reviews* **24**, 1 (2018), pMID: 28548628, <https://doi.org/10.1089/ten.teb.2017.0127>.
 - [19] S. Chandrasekhar, Brownian motion, dynamical friction and stellar dynamics, *Reviews of Modern Physics* **21**, 383 (1949).
 - [20] J. Weber, Fluctuation dissipation theorem, *Physical Review* **101**, 1620 (1956).
 - [21] S. Nawaz, P. Sánchez, K. Bodensiek, S. Li, M. Simons, and I. A. T. Schaap, Cell visco-elasticity measured with afm and optical trapping at sub-micrometer deformations, *PLOS ONE* **7**, 1 (2012).
 - [22] M. F. Brown, Curvature forces in membrane lipid-protein interactions, *Biochemistry* **51**, 9782 (2012).
 - [23] J. Toyjanova, E. Bar-Kochba, C. López-Fagundo, J. Reichner, D. Hoffman-Kim, and C. Franck, High resolution, large deformation 3D traction force microscopy, *PLOS ONE* **9**, 1 (2014).
 - [24] A. Grinthal, I. Adamovic, B. Weiner, M. Karplus, and N. Kleckner, Pr65, the HEAT-repeat scaffold of phosphatase PP2A, is an elastic connector that links force and catalysis, *Proceedings of the National Academy of Sciences* **107**, 2467 (2010), <https://www.pnas.org/doi/pdf/10.1073/pnas.0914073107>.
 - [25] K. Elamvazhuthi and S. Berman, Mean-field models in swarm robotics: a survey, *Bioinspiration and Biomimetics* **15**, 015001 (2019).
 - [26] C. W. Reynolds, Flocks, herds and schools: A distributed behavioral model, in *Proceedings of the 14th Annual Conference on Computer Graphics and Interactive Techniques*, SIGGRAPH '87 (Association for Computing Machinery, New York, NY, USA, 1987) pp. 25–34.
 - [27] C. M. Nelson, Geometric control of tissue morphogenesis, *Biochimica et Biophysica Acta - Molecular Cell Research*

- 1793, 903 (2009).**
- [28] P. W. Ellis, K. Nayani, J. P. McInerney, D. Z. Rocklin, J. Park, M. Srinivasarao, E. A. Matsumoto, and A. Fernandez-Nieves, Curvature-induced twist in homeotropic nematic tori, *Phys. Rev. Lett.* **121**, 247803 (2018).
 - [29] F. Zorilla, M. Ritter, J. Sappl, W. Rauch, , and M. Harders, Accelerating surface tension calculation in sph via particle classification and monte carlo integration, *Computers* **9** (2020).
 - [30] R. Barretta, F. Marotti de Sciarra, and M. S. Vaccaro, On nonlocal mechanics of curved elastic beams, *International Journal of Engineering Science* **144**, 103140 (2019).
 - [31] J. M. Barakat and T. M. Squires, Curvature-mediated forces on elastic inclusions in fluid interfaces, *Langmuir* **38**, 1099 (2022).
 - [32] H. J. Johnson, M. McCormick, and L. Ibanez, *The ITK Software Guide Book 1: Introduction and Development Guidelines*, fourth edition. updated for itk version 4.13.0 ed. (Kitware, Inc., 2019).
 - [33] R. B. Rusu and S. Cousins, 3D is here: Point Cloud Library (PCL), in *2011 IEEE International Conference on Robotics and Automation* (2011) pp. 1–4.
 - [34] M. Janiszewska, M. C. Primi., and T. Izard, Cell adhesion in cancer: Beyond the migration of single cells, *J Biol Chem* **295**, 2495 (2020).
 - [35] E. Fix and J. L. Hodges, Discriminatory analysis. nonparametric discrimination: Consistency properties, USAF School of Aviation Medicine (1951).
 - [36] J. Bentley, Multidimensional binary search trees used for associative searching, *ACM* **18**, 509 (1975).
 - [37] I. Jolliffe and J. Cadima, Principal component analysis: a review and recent developments, *Phil. Trans. R. Soc. A.* **374** (2016).
 - [38] I. Kleino, P. Frolovaitė, T. Suomi, and L. L. Elo, Computational solutions for spatial transcriptomics, *Phil. Trans. R. Soc. A.* **20**, 4870 (2022).
 - [39] J. Anzola, J. Pascual, G. Tarazona, and G. C. R., A clustering wsn routing protocol based on k-d tree algorithm, *Sensors* **18**, 2899 (2018).
 - [40] X. Li, L. Tao, C. S. Levin, and L. R. Furenlid, Fast gamma-ray interaction-position estimation using k-d tree search, *Phil. Trans. R. Soc. A.* **64**, 155018 (2019).
 - [41] W. R. Burk, S. L. Flegler, and W. M. Hess, A clustering wsn routing protocol based on k-d tree algorithm, *Mycologia* **74**, 166 (1982).
 - [42] N. M. Anderson and M. C. Simon, The tumor microenvironment, *Current Biology* **30**, 921 (2020).
 - [43] P. Savagner, The epithelial–mesenchymal transition (emt) phenomenon, *Annals of Oncology* **21**, viii89 (2010), educational Book of the 35th ESMO Congress Milan, Italy 8–12 October 2010.
 - [44] A. Moustakas and A. G. de Herreros, Epithelial–mesenchymal transition in cancer, *Molecular Oncology* **11**, 715 (2017), <https://febs.onlinelibrary.wiley.com/doi/pdf/10.1002/1878-0261.12094>.
 - [45] C. W. Reynolds, Flocks, herds and schools: A distributed behavioral model, *SIGGRAPH Comput. Graph.* **21**, 25 (1987).
 - [46] H. Coxeter, *Projective Geometry* (University of Toronto Press, 1974).
 - [47] A. I. Bobenko and I. Izmestiev, Alexandrov’s theorem, weighted delaunay triangulations, and mixed volumes, *Annales de l’institut Fourier* **66**, 447 (2016).
 - [48] D. Marenduzzo, *The Physics of DNA and Chromosomes* (IOP Publishing, 2018).
 - [49] M. A. Soler and P. F. Faísca, Effects of knots on protein folding properties, *PLoS One* **8** (2013).
 - [50] H. Schubert, *Kalkül der abzählenden Geometrie* (Springer, 1879).